CONJUGATED HEAT TRANSFER SIMULATION OF BUOYANCY-INDUCED FLOW AND HEAT TRANSFER MECHANISMS IN A COMPRESSOR CAVITY

Menghua Jian[1], Yu Xiao[2], Xianda Cheng[3], Wei Dong*

School of Mechanical Engineering, Shanghai Jiao Tong University, Shanghai, 200240, China

Abstract

The variation in blade-tip clearance throughout the flight cycle is primarily influenced by the radial expansion of the compressor rotor, which necessitates an understanding of the radial distribution of temperature and stress in the disks. This study combines conjugate heat transfer simulation with unsteady Reynolds-Averaged Navier-Stokes (URANS) equations to explore the flow and heat transfer mechanisms within a rotating compressor cavity driven by centrifugal buoyancy-induced convection. The numerical results are analyzed in detail and compared with the available experimental data. Using Proper Orthogonal Decomposition (POD) method is utilized to identify coherent structures in the flow field. Furthermore, the effects of rotational Reynolds number, buoyancy parameter, and Rossby number on the radial temperature distribution of the disks were investigated. Results demonstrate the effectiveness of the POD method in capturing the motion state of a pair of unsteady large-scale cyclonic/anticyclonic circulations at the high radius of the cavity. Moreover, the conjugated heat transfer simulation proves valuable in facilitating detailed design computations for selecting the optimized design.

Keywords: Conjugate heat transfer; Unsteady flow; Centrifugal buoyancy-driven convection; Axial throughflow; Proper orthogonal decomposition

1. Introduction

The compressor rotating cavity is a critical component within the secondary air system of areo-engines, exerting significant influence on the performance and stability of both compressor components and the overall engine. Figure 1 illustrates the rotating cavities of a typical high-pressure compressor rotor, where axial throughflow is directed between the shaft and the disks. The flow inside such rotating cavities is dominated by centrifugal buoyancy-induced convection, exhibiting three-dimensional, unsteady, and unstable behavior. In addition, the buoyancy-induced flow presents a strongly conjugate problem, wherein the temperature distribution on the disks influences the flow inside the cavity, and conversely, the flow affects the temperature distribution. As a result, accurately computing or measuring the heat transfer from the solid surfaces to the air poses challenges.

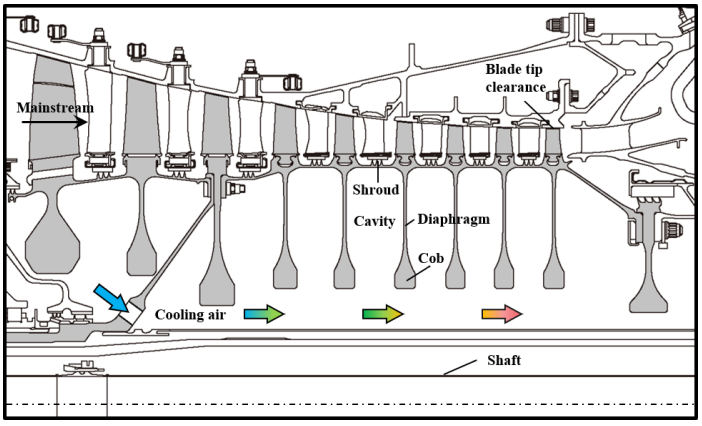

Figure 1 – A Cross-Section of a High-Pressure Compressor Rotor

Experimental studies have been conducted to investigate the flow characteristics inside the rotating cavity with axial throughflow of cooling air. Farthing et al. [1] and Bohn et al. [2] conducted flow visualization using laser Doppler anemometry (LDA) measurements to investigate the flow structures within the rotating cavity. They observed similar flow phenomena under different conditions: cooling air flows radially outward in a radial arm, forming cyclonic and anticyclonic vortex regions. The rotational speed of these vortex structures was approximately 88% to 90% of the disk's rotational speed. Fazeli et al. [3] performed frequency spectral analysis on transient velocity measurements. The significant peaks observed in the power spectra reveal periodicity in the flow structures, indicating that the number of vortex pairs varies over time. Jackson et al. [4] used high-frequency pressure sensors to measure unsteady wall static pressure and analyzed the coherency of the vortex pair within the cavity through spectral analysis. Owen and Long [5] provided a comprehensive review of experimental studies on buoyancy-induced flow in rotating cavities. They indicated that for a given geometry, the non-dimensional parameters Gr, Re_{φ}, Ro, and $\beta\Delta T$ were the most critical factors.

Numerical simulation studies of the rotating cavity with axial throughflow of cooling air also revealed the presence of large-scale flow structures. Tan et al. [6] compared the computational accuracy of various numerical simulation methods, including LES, URANS, and RANS, and found that the URANS method shows reasonable consistency with flow visualization results [2], making it suitable for engineering optimization. Gao et al. [7] used the more advanced wall-modeled large-eddy simulation (WMLES) to further elucidate the details of the flow field.

Proper Orthogonal Decomposition (POD) is a typical modal analysis method that replaces the time-series flow field with multiple basis modes, each containing high-dimensional flow field characteristics of a certain energy level. Lumley et al. [8] introduced POD into turbulence research to identify coherent structures within the flow field. Sirovich et al. [9] proposed the snapshot POD method, using a temporal correlation matrix instead of a spatial one, which simplifies handling complex flow fields and reduces computational costs, thus promoting the widespread application of the POD method. The above review indicates that the flow within the compressor disk cavity exhibits unsteady characteristics. Therefore, the POD method can be employed to identify flow field modes within rotating cavities. This approach facilitates the analysis of flow phenomena and the reconstruction of flow field.

This paper aims to provide a comprehensive analysis of the flow and heat transfer mechanisms inside a rotating cavity with axial throughflow under engine operating conditions. The computational model utilized in this study is based on an engine-representative compressor cavity. A feasible conjugate heat transfer simulation is conducted to investigate the heat transfer characteristics in both the solid and fluid domains. Additionally, the POD method is employed to decompose the unsteady flow field at the axial mid-plane of the rotating cavity with axial throughflow, extracting the dominant velocity and temperature modes. Furthermore, the effects of the rotational Reynolds number, buoyancy parameter, and Rossby number on both the flow field inside the rotating cavity and the radial temperature distribution of the disks are comprehensively analyzed. The detailed analysis of the flow and heat transfer characteristics within the rotating compressor cavity in this paper can provide data for the radial distribution of temperature under different working conditions.

2. Numerical Methods

2.1 Governing Equations

For flows in a non-inertial reference frame with a constant angular velocity ω, additional momentum sources should be considered to accurately capture the effects of the Coriolis force and the centrifugal force. The governing equations in a rotating reference frame are expressed as follows:

$$\frac{\partial \rho}{\partial t} + \nabla \cdot \rho \vec{v}_r = 0 \tag{1}$$

$$\frac{\partial (\rho \vec{v}_r)}{\partial t} + \nabla \cdot (\rho \vec{v}_r \vec{v}_r) + \rho(2\vec{\omega} \times \vec{v}_r + \vec{\omega} \times \vec{\omega} \times \vec{r}) = -\nabla p + \nabla \bar{\bar{\tau}}_r + \vec{F} + \rho \vec{g} \tag{2}$$

$$\frac{\partial (\rho E_r)}{\partial t} + \nabla \cdot (\rho \vec{v}_r H_r) = \nabla \cdot (k \nabla T + \bar{\bar{\tau}}_r \cdot \vec{v}_r) + S_h \tag{3}$$

where ρ, p, $\vec{v}_r$, H_r, and T represent the density, pressure in the system, relative velocity in the rotating reference frame, rothalpy, and temperature, respectively. In addition, $\bar{\bar{\tau}}_r$ denotes the viscous stress tensor, which is calculated by the following formula:

$$\bar{\bar{\tau}}_r = \mu\left[\left(\nabla\vec{v}_r + \nabla\vec{v}_r{}^T\right) - \frac{2}{3}\nabla\cdot\vec{v}_r I\right] \quad (4)$$

where μ and I represent the dynamic viscosity and Kronecker symbol, respectively.
The k-ω SST turbulence model is validated to be substantially suitable for simulating the buoyancy-dominated rotating cavities problem, and has great advantages in predicting the heat transfer performance [3]. This turbulence model encompasses both the k-ε and k–ω models and benefits from automatic near wall treatment that switches to low-Reynolds number formulation in the viscous sublayer. Consequently, the k-ω SST turbulence model has been employed for the simulations.

2.2 Numerical Models

This study considers the rotating compressor cavity rig established at the University of Bath, with detailed information regarding the specific structure and dimensions of the numerical calculation model available in Ref. [10]. The radii of the shroud, disk bore, and shaft are 0.24 m, 0.07 m, and 0.052 m, respectively. The axial distance between disks is 0.04 m. In this study, a full 360-degree model is utilized for the computational domain. The inlet is set 3.8 times the hydraulic diameter (d_h) upstream of the upstream disk cob, while the outlet is placed at 4.2 d_h downstream of the downstream disk cob. Fig.2 illustrates the meridional plane of the computational grid employed, comprising approximately 3,080,000 elements in total. The mesh encompasses both the solid domain of the corotating discs (depicted in grey) and the fluid domain of the axial throughflow (depicted in blue). These two domains are connected by an interface, where coupled heat transfer occurs. The resulting volume grids are all-hexahedral element meshes with refined grids near the wall to obtain reasonable numerical results. Due to the use of the k-ω SST turbulence model in the simulation, the range of y+ on the walls is less than 1 within all the cases.

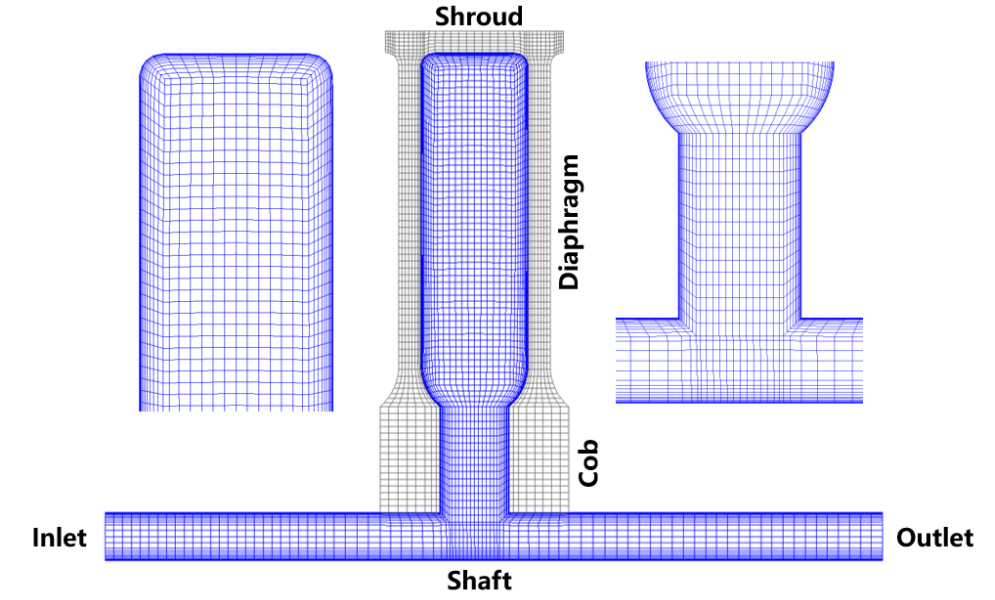

Figure 2 – The computational Grid.

2.3 Numerical Conditions and Boundaries

The 3D viscous unsteady RANS equations, along with the k-ω SST turbulence model, are solved using the SIMPLE algorithm. The simulations are conducted with second order upwind discretization for momentum and turbulence. The Full Buoyancy Model is used to take the buoyancy effects into account. The density of cooling air is calculated using the ideal gas law, and the viscosity is determined using Sutherland's law. The material of the disks is Titanium (Ti-6Al-4V). All simulations are initialized with steady RANS solutions, and a time step of 0.5ms is employed for the unsteady solution.
The boundary conditions are set as follows: the pressure boundary conditions are applied to both inlet and outlet locations in all cases. The absolute pressure at the outlet is fixed. The shroud surface is subjected to a constant heat flux, while the shaft and other outer surfaces of the disks are assumed to be adiabatic. No-slip conditions are set on the solid walls with the corresponding angular speeds.

Before delving into a detailed analysis of the flow mechanisms, this section addresses the accuracy of the numerical simulations. The numerical results are compared with published experimental data for 6000 rpm operating condition [7,11]. In the URANS calculations, the inlet total pressure is adjusted to approximately match the measured mass flow rate, resulting in a relative error of 1.07%. The heat flux of shroud is also adjusted to match the measured inner wall temperature T_b, with a relative error in the buoyancy parameter $\beta\Delta T$ of 1.68%. The calculated rotational speed of the vortex structure is approximately 0.882 times the cavity speed, demonstrating excellent agreement with the experimental results.

The average static temperature of the bore flow is measured at two axial positions between the cobs and the shaft, as depicted in the left subplot of Figure 3. The right subplot of Figure 3 compares the URANS results with the experimental measurements [11]. The numerical results closely align with the experimental data, indicating that the computational method employed in this study is capable of accurately capturing the flow phenomena in the rotating cavity with axial throughflow.

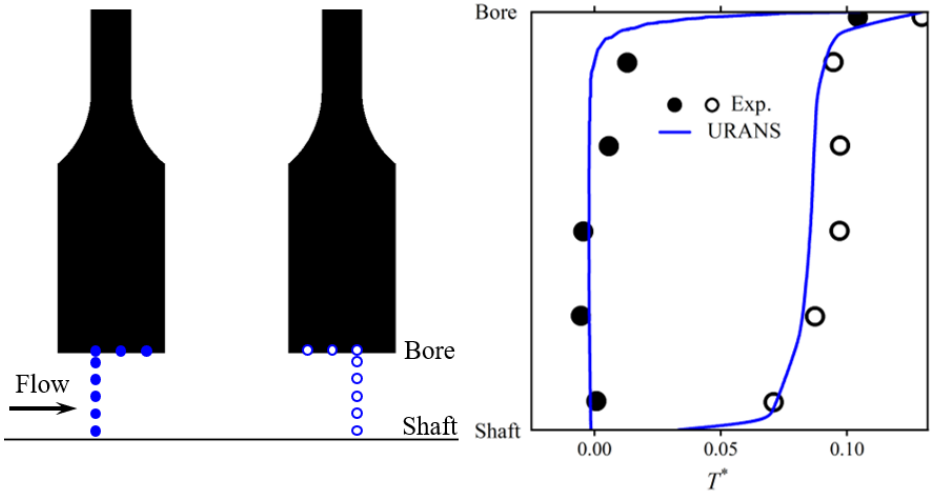

Figure 3 – Validation of numerical methods（6000 rpm).

2.4 Proper Orthogonal Decomposition

Proper Orthogonal Decomposition (POD) is a model reduction technique used to identify the characteristics of the flow field through data representation. The transient flow field characteristics calculated by the numerical method proposed in Section 2.3 for all operating conditions training samples $\boldsymbol{P}^{(i)}$, $i = 1,2,\cdots,n$, are used to construct the matrix $\boldsymbol{U}$ based on the snapshot method developed by Sirovich [9], as follows:

$$\boldsymbol{U} = \begin{bmatrix} V_{11} & V_{12} & \cdots & V_{1i} & \cdots & V_{1n} \\ V_{21} & V_{22} & \cdots & V_{2i} & \cdots & V_{2n} \\ \vdots & \vdots & \vdots & \vdots & \vdots & \vdots \\ V_{l1} & V_{l2} & \cdots & V_{li} & \cdots & V_{ln} \\ T_{11} & T_{12} & \cdots & T_{1i} & \cdots & T_{1n} \\ T_{21} & T_{22} & \cdots & T_{2i} & \cdots & T_{2n} \\ \vdots & \vdots & \vdots & \vdots & \vdots & \vdots \\ T_{l1} & T_{l2} & \cdots & T_{li} & \cdots & T_{ln} \end{bmatrix} \quad i = 1,2,\cdots,n \tag{5}$$

where the ith column of $\boldsymbol{U}$ represents the flow and heat transfer characteristics in terms of core velocity and core temperature at l grid points corresponding to $P^{(i)}$. n is the total number of snapshots. The approximation of snapshot $\boldsymbol{U}^{(i)}$ can be considered as a constrained optimization problem:

$$\begin{gathered} \min_{\Phi|_{j=1}^{m}} \sum_{i=1}^{n} \left\| U^{(i)} - \hat{U}^{(i)} \right\|^2 \\ s.t.\ \left(\Phi^{(i)}, \Phi^{(j)}\right) = \delta_{ij} \quad i,j = 1,2,\cdots,m \end{gathered} \tag{6}$$

where Φ is basis mode extracted from the snapshot matrix, $\hat{U}^{(i)}$ is the approximation of $U^{(i)}$.

Among the various decompositions, Singular Value Decomposition (SVD) is particularly important.

It factorizes the snapshot matrix $\boldsymbol{U}$ into the product as:

$$U = \Phi \Sigma V^T \tag{7}$$

where the $2l \times 2l$ unitary matrix Φ consists of the eigenvectors of UU^T. The $n \times n$ unitary matrix $\boldsymbol{V}$ consists of the eigenvectors of $U^T U$. The $2l \times n$ diagonal matrix Σ contains the singular values arranged in descending order of magnitude, corresponding to the square roots of the eigenvalues λ of UU^T.

The columns of Φ are determined as the POD basis modes $\Phi^{(i)}$. Generally, the first several basis modes can capture most of the features of the snapshot matrix. The proportion of features captured by these modes is represented by E, defined as follows:

$$E = \frac{\sum_{j=1}^{m} \lambda_j}{\sum_{i=1}^{n} \lambda_i} \tag{8}$$

However, the number of basis modes to be retained should be determined not only by E but also by the system characteristics. The snapshot $U^{(i)}$ can be reconstructed by linearly combining the basis modes:

$$U^{(i)} = \sum_{j=1}^{m} b_j{}^{(i)} \Phi^{(j)} \tag{9}$$

where $m < n$. The coefficients $b^{(i)} = [\, b_{i0} \;\; b_{i1} \;\; \cdots \;\; b_{im}]$ are obtained as following:

$$b_j^{(i)} = \left(U^{(i)}, \Phi^{(j)}\right) \;\; i = 1,2,\cdots,n;\; j = 1,2,\cdots,m \tag{10}$$

The coefficient matrix $\boldsymbol{b} = \left[b_1^{(i)}\, b_2^{(i)} \cdots b_m^{(i)}\right]$ is obtained by solving the above equation for all n snapshots. The relationship between the training sample $\boldsymbol{P}^{(i)}$ and the snapshot $\boldsymbol{U}^{(i)}$ can then be approximated by the relationship between $\boldsymbol{P}^{(i)}$ and $b^{(i)}$.

The URANS computational results are recorded at a sampling frequency of 2000 Hz, extracting 2000 snapshots of the flow field for each operating condition. Subsequently, the POD method is applied to decompose the absolute velocity and temperature at the axial mid-plane of the rotating cavity into modes.

3. Computational Results and Analysis

3.1 Flow and Heat Transfer Mechanisms

Figure 4 shows the evolution of the flow structure in the axial mid-plane of the rotating cavity with axial throughflow at $Ro = 0.27$, $\beta\Delta T = 0.37$, $Re_\omega = 3.42 \times 10^6$. The instantaneous flow structures are observed at five equally spaced time intervals within one quasiperiodic in the rotating frame of reference.

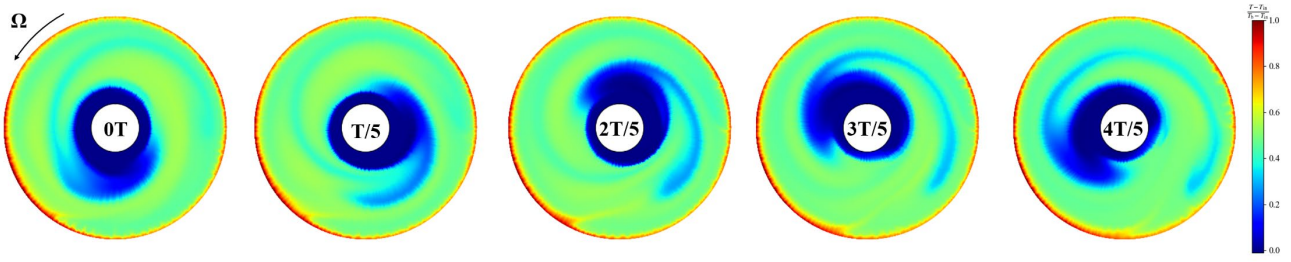

(a) Dimensionless temperature distribution (One quasiperiodic)

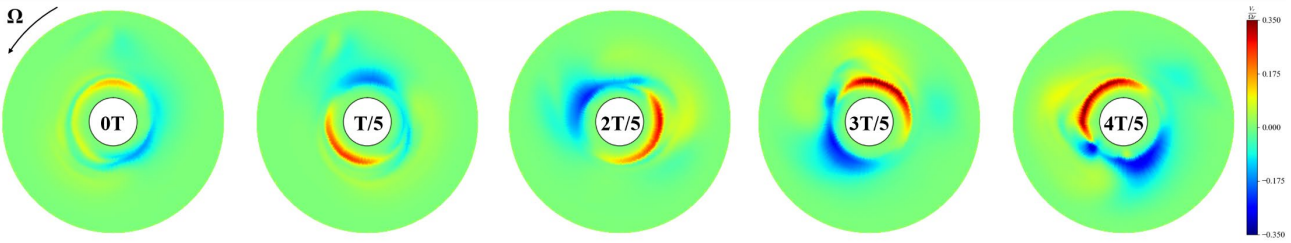

(b) Dimensionless radial velocity distribution (One quasiperiodic)

Figure 4 – Computed time-sequence of contours in mid-axial plane.

Figure 4(a) presents the dimensionless temperature distribution in the mid-axial plane, which aligns

with the classic flow pattern observed in prior studies [1]. As the outer shroud is heated, the temperature of the axial throughflow is lower than that of the rotating cavity wall, corresponding to the deep blue zone at the central bore flow region. It can be observed that the cooling air is transported radially outward through a radial arm, and splits into two streams upon reaching the periphery of the cavity, forming a thin layer that engages in convective heat transfer with the shroud. The results indicate that the radial arm rotates at a speed slightly lower than that of the cavity, and the two streams separated into cyclonic and anticyclonic vortices.

Figure 4(b) presents a dimensionless radial velocity distribution in the mid-axial plane, indicating that the region to the right of the radial arm exhibits cyclonic circulation, rotating in the same direction as the disk, while the region to the left of the radial arm displays anticyclonic circulation, rotating opposite to the disk's rotation. The regions of positive radial velocity correspond to the positions of the radial arms. Radial velocity of cooling air in the bore region is relatively small. Cyclonic and anticyclonic circulations feeds into the bore flow, which subsequently exits through the rotating cavity.

The POD method can be used to obtain the basis modes and corresponding eigenvalues of the unsteady flow field at the axial mid-plane of the rotating cavity with axial throughflow from the snapshot matrix U. As shown in Figure 5, the eigenvalues of the basis modes decay rapidly. It can be observed that lower-order modes possess higher energy and tend to appear in pairs with similar energy levels. The ratio of features contained in the first m basis modes, calculated using Equation (8), reveals that the first POD basis mode accounts for 99.857% of the energy, while the first 6 POD basis modes together contain over 99.95% of the energy. Therefore, this study focuses on analyzing the first six POD basis modes in detail.

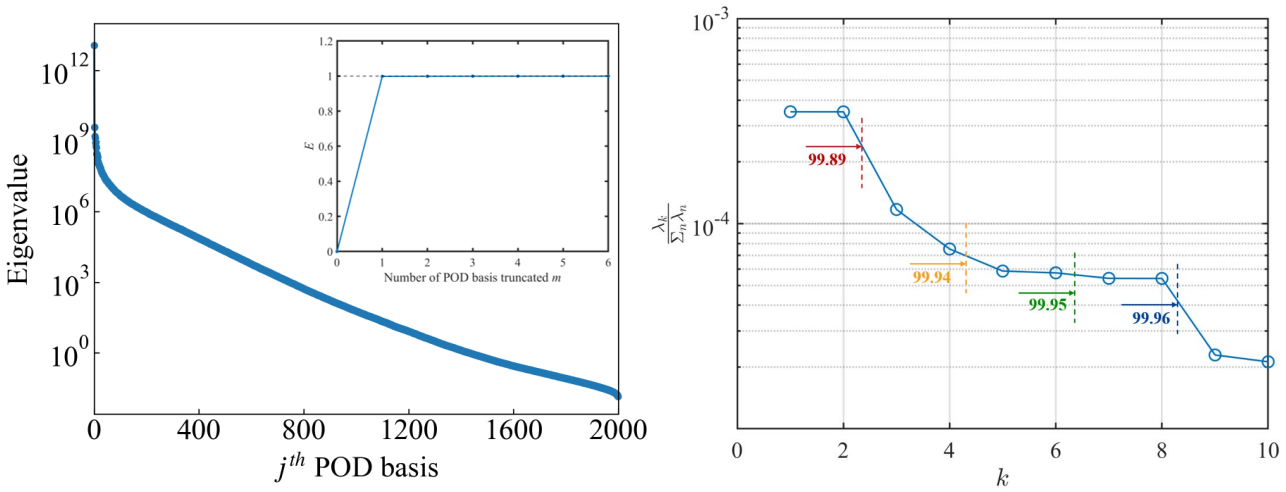

Figure 5 – Eigenvalues and energy captured by the first m POD basis.

Figure 6 illustrates the first six POD basis modes, all of which exhibit rotational symmetry. It can be determined that the first six modes consist of three pairs of conjugate modes. The first, third, and fifth modes share the same spatial distribution as their corresponding even-numbered modes, differing only by a certain phase angle around the rotation axis. Due to their higher energy proportion, Modes 1 and 2 constitute the dominant structures of the transient flow field in a rotating cavity with axial through-flow of cooling air. The first two modes exhibit precession state of large-scale flow structures induced by axial through-flow penetration. Therefore, these modes (the first pair) classified as Precession-Driven modes.

The high-order harmonics of velocity and static temperature can also be uniquely expressed by the corresponding high-order modes, hence the third to sixth order modes are referred to as Resonance Induced modes. The higher-order Resonance-Induced modes primarily represent the complex vortex systems induced between coherent structures within the cavity, corresponding to the higher-order harmonics of the dominant frequency. Based on the energy distribution characteristics, it is believed that the first six modes effectively reflect the main features of quasiperiodic motion of cyclonic/anticyclonic circulations in the rotating cavity.

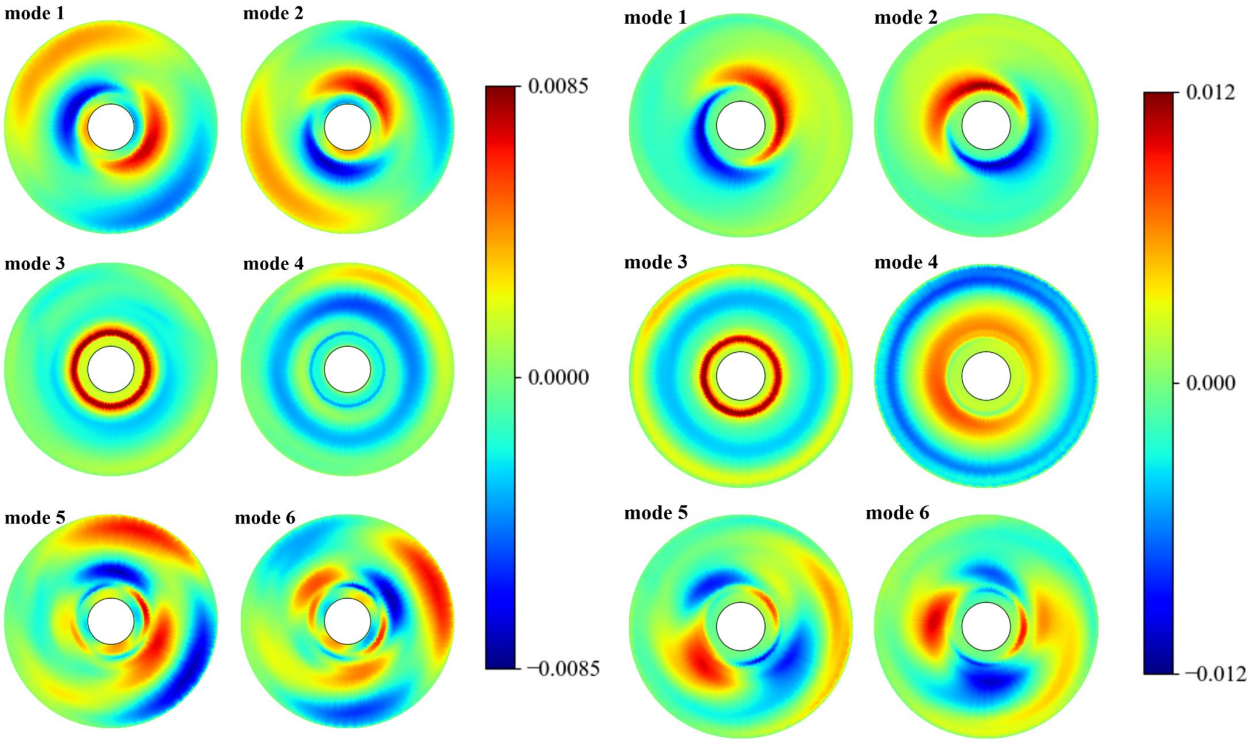

(a) Velocity modes (b) Static temperature modes

Figure 6 – The first six dominant POD modes.

Figure 7 shows the radial distribution of the normalized temperature across the disk. where T_o represents the static temperature of disk surface. T_f is the inlet temperature of axial throughflow. $T_{o,b'}$ is the temperature at the lower edge of the shroud. The axial throughflow is left-to-right; The blue and red lines are for the average radial temperature on the upstream and downstream rotating disks, respectively.

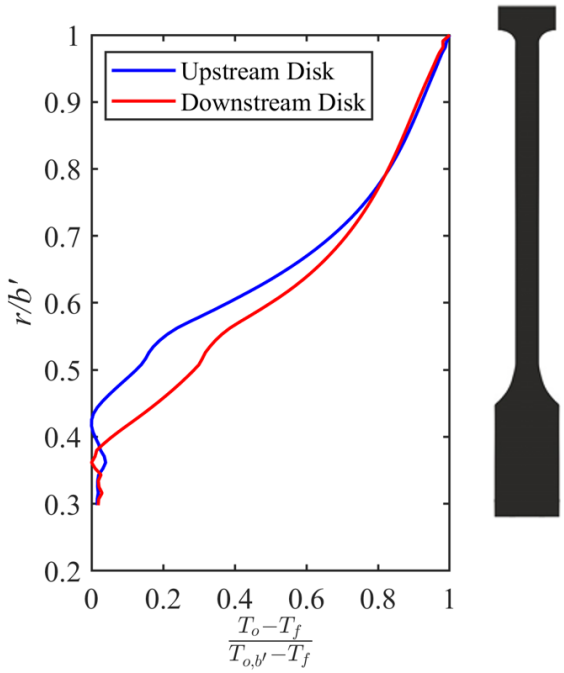

Figure 7 – Nondimensional temperatures on the upstream and downstream disk.

The radial temperature gradient on the rotating disks is distinctly observed and will drive buoyancy-induced flow under this operating condition, where the heat flux on the outer shroud surface equals to 3000 W/m^2. At radii approaching the shroud and for the portion of the diaphragm ($r/b' > 0.8$), the temperature distribution on the upstream and downstream disks is nearly consistent. Close to the bore, especially in the region of the cobs, the downstream disk is slightly hotter than the upstream

one. In the central region of the disk ($0.4 < r/b' < 0.8$), the downstream disk is evidently hotter than the upstream disk. The axial throughflow exhibits a clear rise in temperature due to enthalpy exchange with the rotating cavity and direct heat transfer from the bore of the cobs.

3.2 Influence of Rossby number

The influence of the Rossby number on the nondimensional temperatures of the upstream and downstream disks was investigated by varying the inlet total pressure, while keeping the buoyancy parameter and the rotational Reynolds number constant ($\beta\Delta T = 0.40$, $Re_\omega = 2 \times 10^6$).

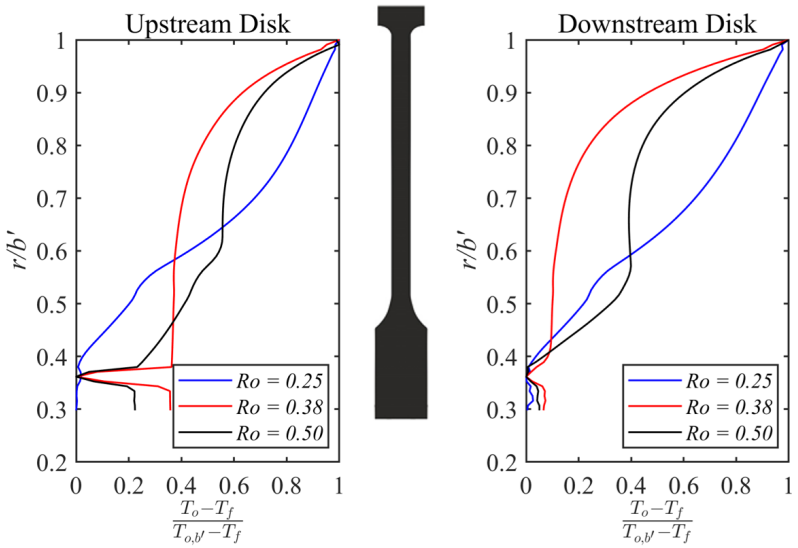

Figure 8 – Nondimensional temperatures on the upstream and downstream disks at different Ro.

Increasing the Rossby number enhances the inertia of axial throughflow, creating a mixing region in the inner area where entrained cooling air mixes with hot fluid, thereby intensifying forced convection. As shown in Figure 8, with the increase in the Rossby number, the dimensionless temperature of the downstream disk decreases dramatically along the radial direction, while the dimensionless temperature in the high-radius region ($r/b' > 0.6$) of the upstream disk also decreases significantly.

3.3 Influence of Buoyancy parameter

This section discusses the impact of buoyancy parameter on the dimensionless temperature distribution of the upstream and downstream disks. This is achieved by varying the heat flux on the outer shroud surface while keeping the Rossby number and rotational Reynolds number constant ($Ro = 0.27$, $Re_\omega = 3.4 \times 10^7$).

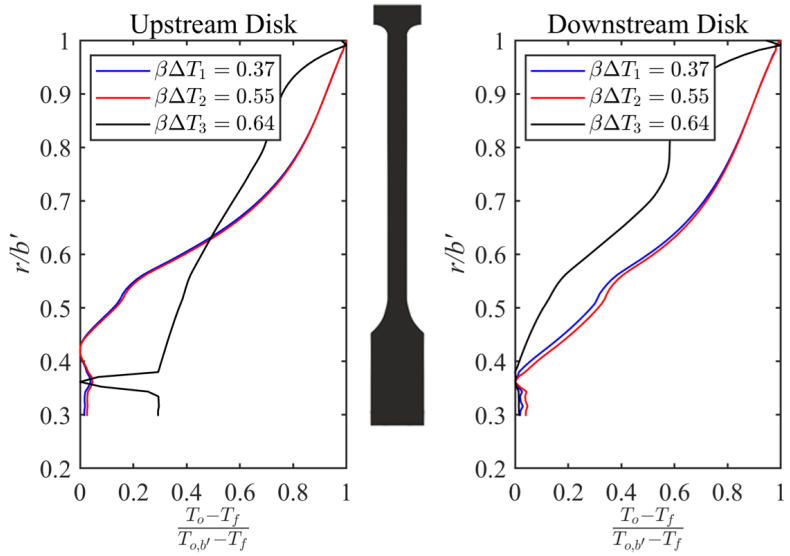

Figure 9 – Nondimensional temperatures on the upstream and downstream disks at different $\beta\Delta T$.

In Figure 9, it is evident that for $\beta\Delta T < 0.55$, the influence of buoyancy parameter on the temperature distribution of the both upstream and downstream disks is quite small. However, for buoyancy parameter exceeding 0.55, the dimensionless temperature of the diaphragm region on the downstream disk notably decreases. This phenomenon is attributable to the fact that $\beta\Delta T$ is proportional to the intensity of natural convection on the disks. An increase in buoyancy parameter enhances the axial throughflow penetration within the cavity, thereby strengthening heat transfer.

3.4 Influence of rotational Reynolds number

Keeping the Rossby number and buoyancy parameter unchanged ($Ro = 0.26$, $\beta\Delta T = 0.40$), the influence of rotational Reynolds number (Re_ω) on the flow field of rotating cavity was carried out by changing the angular velocity of the disks.

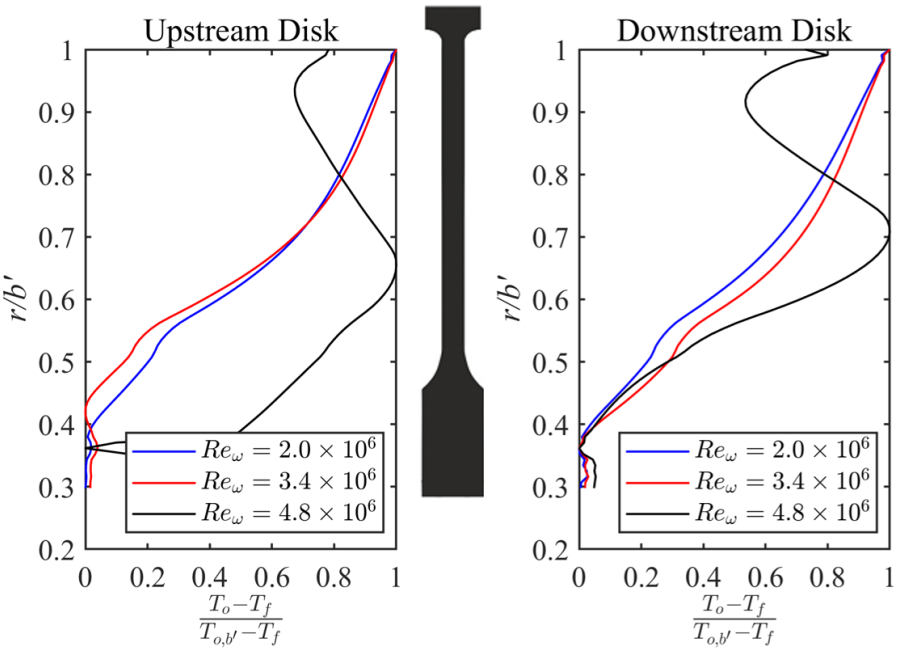

Figure 10 – Nondimensional temperatures on the upstream and downstream disks at different Re_ω.

Figure 10 illustrates that at high rotational speeds, the dimensionless temperature distribution significantly increases on both the upstream and downstream disks in the region of $r/b' < 0.8$. As Re_ω increases, compressibility effects cause the core temperature to rise, which in turn tends to weaken heat transfer.

4. Conclusions

This study presents conjugate heat transfer simulations using URANS equations for a compressor cavity with axial throughflow. The flow field structures were analyzed using Proper Orthogonal Decomposition (POD) method. The temperature distribution on the disk surfaces under different Rossby numbers, buoyancy parameters, and rotational Reynolds numbers were clarified. The conclusions are as follows:

- The conjugated heat transfer simulation method proves valuable in accurately calculating large-scale unsteady flow structures induced by vortex variations.
- The POD method effectively extracts coherent structures from flow field. The Precession-Driven modes exhibit precession state of large-scale flow structures induced by axial through-flow penetration, while the Resonance-Induced modes predominantly captures the complex vortex systems induced by interactions among coherent structures within the cavity.
- Increasing the Rossby number and buoyancy parameter enhances axial inertial forces and natural convection, leading to increased convection and improved heat transfer within the rotating cavity. However, at high rotational Reynolds numbers, enhanced compressibility effects in the air cause the core temperature to rise, thereby deteriorating heat transfer.

Nomenclature

Ro = Rossby number $(= W/\Omega a)$

$\beta\Delta T$ = buoyancy parameter $\left(= \left(T_{o,\mathrm{b}} - T_f\right)/T_f\right)$

Re_ω = rotational Reynolds number $\left(= \rho_f \Omega b^2/\mu_f\right)$

References

[1] Farthing P R, Long C A, Owen J M, et al. Rotating Cavity With Axial Throughflow of Cooling Air: Flow Structure[J]. *Journal of Turbomachinery*, Vol. 114, No. 1,1992.

[2] Bohn D E, Deutsch G N, Simon B, et al. Flow Visualisation in a Rotating Cavity with Axial Throughflow [C]. *Munich: ASME Turbo Expo 2000: Power for Land, Sea, and Air*, 2000.

[3] Fazeli S M, Kanjirakkad V and Long C. Experimental and computational investigation of flow structure in buoyancy-dominated rotating cavities. *Journal of Engineering for Gas Turbines and Power*, Vol. 143, No. 7, 2021.

[4] Jackson R W, Tang H, Scobie J A, et al. Unsteady Pressure Measurements in a Heated Rotating Cavity [J]. *Journal of Engineering for Gas Turbines and Pow*er, Vol. 144, No. 4, 2022.

[5] Owen J M, Long C A. Review of Buoyancy-Induced Flow in Rotating Cavities[J]. *Journal of Turbomachinery,* Vol. 137, No. 11,2015.

[6] Tan Q, Jing R, Jiang H. Prediction of Flow Features in Rotating Cavities with Axial Throughflow by RANS and LES [C]. *Orlando: ASME Turbo Expo 2009: Power for Land, Sea, and Air*, 2009.

[7] Gao F, Chew J W. Flow and heat transfer mechanisms in a rotating compressor cavity under centrifugal buoyancy-driven convection[J]. *Journal of engineering for gas turbines and power*, Vol. 144, No. 5,2022.

[8] Lumley J L. Stochastic Tools in Turbulence [M]. *New York: Courier Corporation*, 2007.

[9] Sirovich L. Turbulence and the dynamics of coherent structures. I. Coherent structures[J]. *Quarterly of applied mathematics*, Vol. 45, No. 3,1987.

[10]Luberti D, Patinios M, Jackson R W, et al. Design and Testing of a Rig to Investigate Buoyancy-Induced Heat Transfer in Aero-Engine Compressor Rotors. *Journal of Engineering for Gas Turbines and Power*, Vol. 143, No. 4,2021.

[11]Jackson R W, Luberti D, Tang H, et al. Measurement and analysis of buoyancy-induced heat transfer in aero-engine compressor rotors[J]. *Journal of Engineering for Gas Turbines and Pow*er, Vol. 143, No. 6, 2021.

Copyright Statement